Supplementary Material: Quantum Imaging Using Entangled Photon Pairs from Nonlinear Metasurface

Jinyong Ma[1†], Jinliang Ren[1†], Jihua Zhang[1,2], Jiajun Meng[3], Caitlin McManus-Barrett[1], Kenneth B. Crozier[3,4], Andrey A. Sukhorukov[1*]

[1]ARC Centre of Excellence for Transformative Meta-Optical Systems, Department of Electronic Materials Engineering, Research School of Physics, The Australian National University, Canberra, 2600, ACT, Australia.
[2]Songshan Lake Materials Laboratory, Dongguan, 523808, P. R. China.
[3]ARC Centre of Excellence for Transformative Meta-Optical Systems, School of Physics, University of Melbourne, Melbourne, 3010, Victoria, Australia.
[4]ARC Centre of Excellence for Transformative Meta-Optical Systems, Department of Electrical and Electronic Engineering, University of Melbourne, Melbourne, 3010, Victoria, Australia.

*Corresponding author(s). E-mail(s): andrey.sukhorukov@anu.edu.au;
†These authors contributed equally to this work.

This Supporting Information contains 6 sections and 9 figures, which provide extra details on the theoretical and experimental aspects of our work.

(October 25, 2024)

Contents

S1 Theory of the combined quantum imaging system

S1.1 Concept and modelling

In this work, we propose and experimentally demonstrate a novel imaging protocol that integrates quantum ghost imaging with all-optical scanning, leveraging spatially entangled photon pairs generated from a lithium niobate metasurface. Here we present the theoretical framework underpinning this imaging protocol.

We employ the coupled mode theory formulated in Ref. (*S1*) to derive the full spatial emission function $\Xi(\lambda_p, k_y^{(s)}, k_z^{(s)}, k_y^{(i)}, k_z^{(i)})$ of the photon pairs generated from the metasurface, where $k_y^{(s)}, k_z^{(s)}, k_y^{(i)}, k_z^{(i)}$ are the transverse wave vectors of the signal and idler photons along the $y-$ and $z-$ directions. The pump beam wavelength λ_p is included as a variable of the emission function due to its influence on the photon emission pattern. The explicit expression for Ξ can be found in the Supplementary Eq. (S19) of Ref. (*S1*).

To capture a complete description of the imaging protocol, we consider a Gaussian pump laser whose beam profile in the k-space at the metasurface is described by

$$F_G(k_y^{(p)}, k_z^{(p)}) = \frac{w_p}{\sqrt{4\pi}} \exp\left[-w_p^2 \frac{(k_y^{(p)})^2 + (k_z^{(p)})^2}{4}\right], \tag{S1}$$

where w_p is the pump beam waist and $k_{y,z}^{(p)}$ are its transverse wave vectors. Applying the transverse phase matching conditions $k_{y,z}^{(p)} = k_{y,z}^{(s)} + k_{y,z}^{(i)}$, the photon emission Ξ_G can be written as

$$\begin{aligned}\Xi_G(\lambda_p, k_y^{(s)}, k_z^{(s)}, k_y^{(i)}, k_z^{(i)}) &= F_G(k_y^{(p)}, k_z^{(p)})\Xi(k_y^{(s)}, k_z^{(s)}, k_y^{(i)}, k_z^{(i)}) \\ &= \frac{w_p}{\sqrt{4\pi}} \exp\left[-w_p^2 \frac{(k_y^{(i)} + k_y^{(s)})^2 + (k_z^{(i)} + k_z^{(s)})^2}{4}\right] \Xi(\lambda_p, k_y^{(s)}, k_z^{(s)}, k_y^{(i)}, k_z^{(i)}).\end{aligned} \tag{S2}$$

We now analyze the imaging of a binary object, where each pixel transmission value is set as 0 or 1. Here 0 or 1 represents opaque or transparent regions, respectively. The object is placed in the signal arm of the setup presented in Fig. 1 of the main paper, and its spatial profile is denoted as $O_s(k_y^{(s)}, k_z^{(s)})$. In the idler arm, we introduce a completely transparent object function $O_i(k_y^{(i)}, k_z^{(i)}) = 1$ (every pixel has a value of 1) because there is no object in this arm. The overall profile function for the object is therefore defined as $O(k_y^{(s)}, k_z^{(s)}, k_y^{(i)}, k_z^{(i)}) = O_s(k_y^{(s)}, k_z^{(s)}) \otimes O_i(k_y^{(i)}, k_z^{(i)})$. Then, the spatial function of the biphoton after interacting with the object becomes:

$$U_G(\lambda_p, k_y^{(s)}, k_z^{(s)}, k_y^{(i)}, k_z^{(i)}) = O(k_y^{(s)}, k_z^{(s)}, k_y^{(i)}, k_z^{(i)})\Xi_G(\lambda_p, k_y^{(s)}, k_z^{(s)}, k_y^{(i)}, k_z^{(i)}). \tag{S3}$$

The photons transmitted through the object are collected with single-photon detectors. Specifically, the signal photons are collected by a single-pixel bucket detector and the idler photons are measured by a 1D detector array along the z-direction. We then analyze the correlations between the bucket detector and the n_z-th (where $n_z = 1, 2, 3, 4...$) pixel of the detector array. The coincidence rate for the n_z-th correlation measurement can be obtained

Eigenfrequencies at normal incidence, THz			
$\omega_1/(2\pi)$	$\omega_2/(2\pi)$	$\omega_3/(2\pi)$	$\omega_4/(2\pi)$
188.84	189.23	205.35	206.26
Loss coefficients at normal incidence, THz			
$\gamma_1/(2\pi)$	$\gamma_2/(2\pi)$	$\gamma_3/(2\pi)$	$\gamma_4/(2\pi)$
0	0.18	0.23	0
Coupling coefficients, THz·μm			
$V_{12}/(2\pi)$	$V_{34}/(2\pi)$	$C_{13}/(2\pi)$	$C_{24}/(2\pi)$
22.67	22.65	-1.17	-1.28
Coupling coefficients, THz·μm^2			
$U_{12,y}/(2\pi)$	$U_{34,y}/(2\pi)$	$U_{12,z}/(2\pi)$	$U_{34,z}/(2\pi)$
-0.18	-0.69	1.62	1.54
Nonlinear coefficients, $(\mu m^2/mW)^{1/2}$			
η_1	η_2	η_3	η_4
1.98×10^{-5}	1.98×10^{-5}	0	0

Table S1 Coefficients of coupled-mode theory. The values are obtained through the fitting of the coupling matrix to the finite-element simulations of the fabricated metasurface.

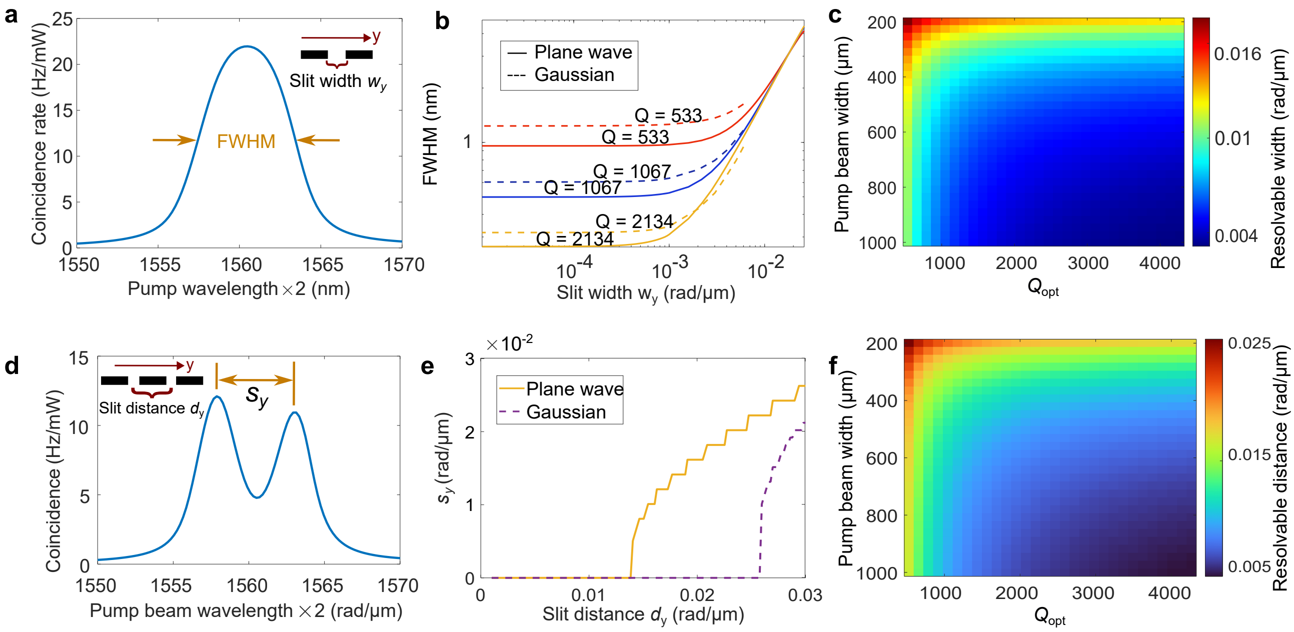

Figure S1 Predicted resolution of all-optical scanning imaging in the y-direction. **a**, Optical scanning imaging of an object with one open slit along the y-direction. The object is placed in the signal arm of Fig. 1**a** of the main paper. The photon emission scans through the object along the y-direction as the pump wavelength varies. This measurement exhibits a peak with a characteristic full width at half maximum (FWHM) of the peak as sketched in the plot. The FWHM can be used to extract the value of slit width w_y. **b**, FWHM vs. slit width w_y. As the slit width gets narrower, the FWHM of the coincidence peak in panel **a** decreases. The minimum resolvable slit width is defined as the slit width at which the FWHM starts to saturate at its lower limit. **c**, Minimum resolvable slit width vs. pump beam waist $w_\mathbf{p}$ and Q_opt. **d**, Optical scanning imaging of an object with two open slits. The two coincidence peaks at a separation s_y reveal the information of the slit distance d_y. **e**, Peak separation s_y vs. slit distance d_y. For an object containing two slits, the two coincidence peaks become indistinguishable from each other (i.e., $s_y \approx 0$) as two slits get closer to a certain threshold, which defines the minimum resolvable distance. **f**, Minimum resolvable distance vs. the pump beam waist and Q_opt.

by integrating the biphoton function $U_G(\lambda_p, k_y^{(s)}, k_z^{(s)}, k_y^{(i)}, k_z^{(i)})$ over $k_y^{(s)}, k_z^{(s)}, k_y^{(i)}$ for the whole collection range and $k_z^{(i)}$ for the specific range δ_z covered by the n_z-th pixel of the detector array. This coincidence rate is given by

$$C(\lambda_p, n_z) = \int_{k_{y,\min}^{(s)}}^{k_{y,\max}^{(s)}} \int_{k_{z,\min}^{(s)}}^{k_{z,\max}^{(s)}} \int_{k_{y,\min}^{(i)}}^{k_{y,\max}^{(i)}} \int_{k_{z,\min}^{(i)}+(n_z-1)\delta_z}^{k_{z,\min}^{(i)}+n_z\delta_z} dk_y^{(s)} dk_z^{(s)} dk_y^{(i)} dk_z^{(i)} U_G. \tag{S4}$$

The coincidence function $C(\lambda_p, n_z)$ can then be linearly mapped to reconstruct the image of the object. To ensure the linear mapping, $2 \times \lambda_p$ must be set sufficiently far away from the band edge (i.e., the resonance wavelength at normal incidence) of the optical resonances supported by the metasurface.

In the following simulations, we consider a collection angle of 1.5 degree used in our experiments, which corresponds to the transverse wavevectors $k_y^{(s)}, k_z^{(s)}, k_y^{(i)}, k_z^{(i)} \in [-0.12, 0.12]$ rad/µm. The period and width of the metagrating are optimized to support an optical resonance of 1585 nm at normal incidence, enabling linear control of the photon emission direction across the wavelength tuning range of the pump laser (779-790 nm). The coupled-mode theory coefficients for the metasurface used in this work, as given in Table S1, differ from those in Ref. (*S1*). The estimated quality factor $Q_{\rm opt}$ of the bright mode is ≈ 500 at normal incidence. Additionally, the resonance wavelength of the fabricated metasurface is 1584 nm at $k_y = 0$ (see Fig. 2**a** of the main paper), which is only 1 nm off from that ($\approx$ 1585 nm) of the designed metasurface due to fabrication imperfections.

S1.2 Transverse phase matching for non-degenerate quantum imaging

In Fig. 6 of the main paper, we explore approaches for generating non-degenerate photon pairs from nonlinear metasurfaces. We anticipate that our quantum imaging protocol combining optical scanning and ghost imaging can be extended to non-degenerate regimes. Here we provide additional details about the simulations shown in Figs. 6**b** and 6**d**.

For Fig. 6**b**, non-degenerate photon pairs can be produced by simply tilting the pump beam. The simulation is performed using the coupled-mode theory with the coefficients listed in Table S1. The transverse wavenumber k_p of the pump beam is set as $k_p = 0.81$ rad/µm. The points with different color gradients represent different pump wavelengths from 797.5 nm to 812.5 nm (from darker to lighter).

For Fig. 6**d**, we consider a quasi-periodic metasurface supporting dual optical resonances at both visible and infrared wavelengths. The infrared band is modeled using the coefficients provided in Table S1. The visible band is implemented with eigenfrequencies shifted by 200 THz from the ones in Table S1 while other parameters remain the same. The pump beam is normally incident on the metasurface, with its wavelength being tuned from 502 nm to 514 nm (points with colors from darker to lighter).

S2 Imaging resolution

With the theoretical frameworks developed in Sec. S1, we analyze the resolution of all-optical scanning imaging along y-direction and ghost imaging along z-direction, respectively.

In the y-direction, we first consider an object with an open slit of width w_y. The coincidence counts $C(\lambda_p, n_z = n_0)$ for a specific pixel n_0 of the detector array are calculated for different pump wavelengths λ_p, as shown in Fig. S1**a**. The full-width half maximum (FWHM) of the coincidence peak is employed to calibrate the value of the slit width w_y. Fig. S1**b** presents the dependence of FWHM on the slit width, where the dependence is linear as w_y is greater than a specific threshold $w_{y,\rm res}$ and reaches a plateau at $w_y < w_{y,\rm res}$. The threshold $w_{y,\rm res}$ defines the minimum resolvable slit width that the optical tuning imaging protocol can reach. We find that $w_{y,res}$ can be improved at higher optical quality factors $Q_{\rm opt}$ and larger pump beam waists w_p, as displayed in Fig. S1**b**. The underlying mechanism is that larger $Q_{\rm opt}$ and w_p reduce the k_y range satisfying the transverse phase matching condition, thereby lowering the spatial bandwidth of the emission and increasing the all-optical scanning imaging resolution.

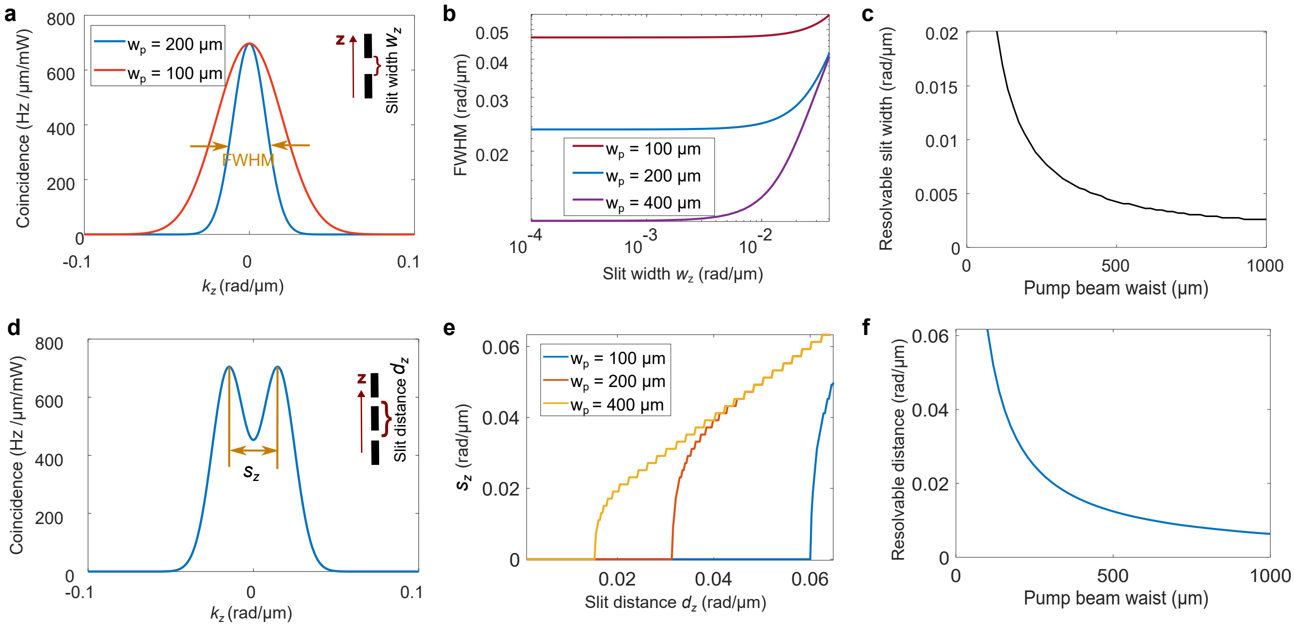

Figure S2 Predicted resolution of quantum ghost imaging in the z-direction. **a**, Quantum ghost imaging of an object with one open slit along the z-direction. As depicted in Fig. 1**a** of the main paper, the signal photons illuminating the object are collected by a bucket detector. Assuming we have a z-oriented 1D detector array with 200 pixels in the idler arm, the correlations between the bucket detector and each pixel at wavenumber k_z of the detector array provide information about the the object. The plot of coincidence vs. k_z presents a peak with a finite FWHM that indicates the slit width w_z. **b**, FWHM vs. slit width w_z. The FWHM reaches saturation at its lower bound for a specific slit width, which is defined as the minimum resolvable slit width. **c**, Minimum resolvable slit width vs. pump beam waist w_p. A smaller minimum resolvable slit width can be realized by increasing the pump beam waist. **d**, Quantum ghost imaging of an object with two open slits. The separation s_z of the two coincidence peaks reveals the information about the distance d_z of the two slits. **e**, Peak separation s_z vs. slit distance d_z. Two coincidence peaks overlap (i.e., $s_z \approx 0$) when the slits approach a certain minimum resolvable distance. **f**, Minimum resolvable distance vs. w_p. The ghost imaging resolution can be optimized using a larger pump beam waist.

Furthermore, we analyze the imaging resolution of an object containing two open slits. The calculation of coincidence vs. $\lambda_p \times 2$ (see Fig. S1**d**) manifests two peaks at a separation s_y, which can be used to extract the information on the distance d_y between the two slits. Here each slit width is set as half of the slit distance, i.e., $w_y = d_y/2$. The dependence of s_y on the slit distance for a plane-wave and a Gaussian pump beam is presented in Fig. S1**e**. The distance can be linearly determined from d_y when the separation is larger than a threshold value $d_{y,\mathrm{res}}$, which is defined as the minimum resolvable distance. Just as the minimum resolvable width $w_{y,\mathrm{res}}$, we can achieve a smaller $d_{y,\mathrm{res}}$ by using a larger Q_{opt} and w_p. In summary, the image of an object with open slits can be reconstructed from the measurements of coincidences vs. λ_p when each slit width is $> w_{y,\mathrm{res}}$ and the respective slit distance is $> d_{y,\mathrm{res}}$.

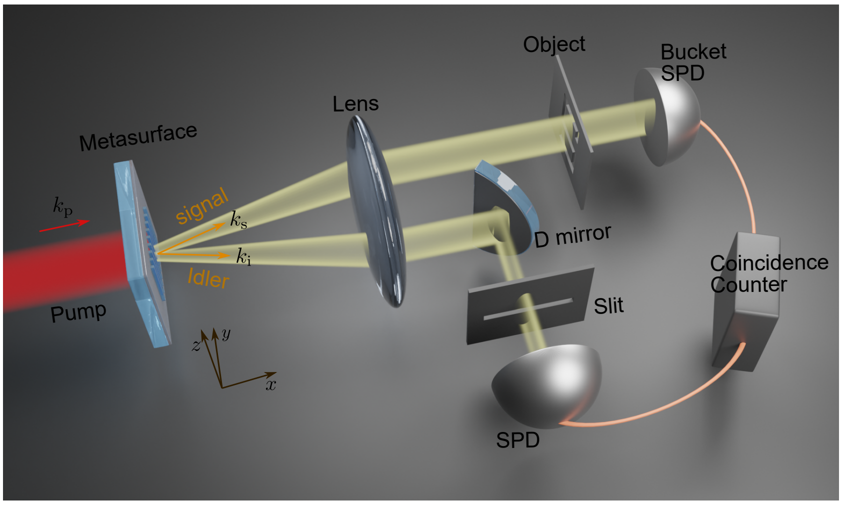

Figure S3 Experimental setup of the combined quantum imaging. The photon pairs generated from the metasurface are collimated with a lens at a focal length of 50 µm and are subsequently split into two optical paths (signal and idler arms) using a "D" shaped mirror. The object is positioned in the Fourier plane of a 2-f imaging system of the signal arm, followed by a bucket single-photon detector (SPD). In the idler arm, a scanning slit translated along the z-axis acts as a tunable detector array. The other SPD collects photons transmitted through the slit. The photons received by the two detectors are converted to electrical signals and are then analyzed by a coincidence counter. The object image is reconstructed through the coincidence measurements at different slit positions and pump laser wavelengths.

We perform a similar resolution analysis for the ghost imaging in the z-direction, as shown in Fig. S2. We simulate the correlations between the bucket detector in the signal arm and the z-oriented 1D detector array with 200 pixels placed in the idler arm. We consider objects with open slits along the z-direction, where the slit width is defined as w_z and the distance between the neighbouring slits denotes d_z. The FWHM and separation (s_z) of coincidence peaks can be used to reconstruct the image of the objects, as shown in Fig. S2**a,d**. We find that the minimum resolvable width and distance do not depend on the quality factor Q_{opt} of the optical resonances, but are determined by the pump beam waist w_p just as in conventional quantum ghost imaging.

S3 Experimental characterization of photon emission

S3.1 Experimental setup

The main paper has briefly described the experimental setup. Here we provide further details as shown in Fig. S3. The photon emission from the metasurface is collimated with a lens of focal length 50 mm, followed by a "D" shaped mirror for splitting the signal and idler photons. The object is placed in the signal arm at the Fourier plane of the metasurface, where the signal and idler photons are spatially anti-correlated. For convenience, we achieve the functionality of the detector array by translating a narrow slit. The signal photons passing through the object and the idler photons transmitting through the slit are received by two single-photon detectors respectively and analyzed by a coincidence counter.

S3.2 SPDC enhancement with the lithium niobate metasurface

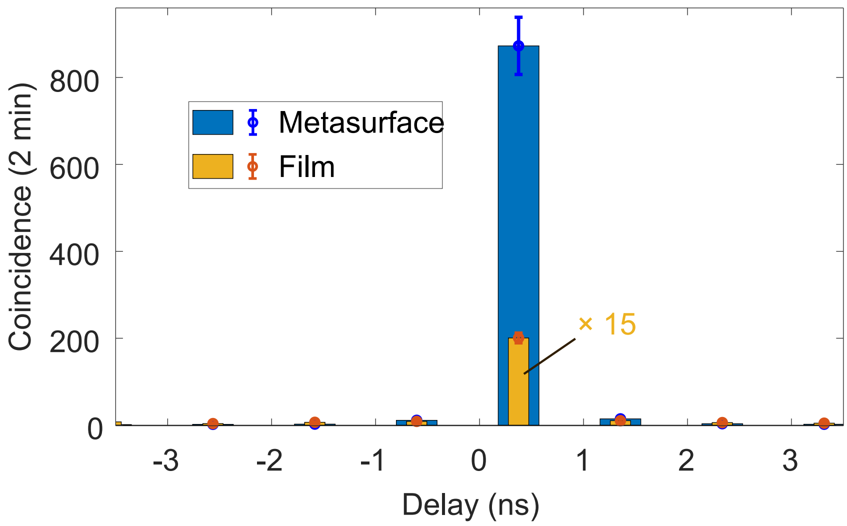

Figure S4 The coincidence rate of photon pairs generated from lithium niobate nonlinear metasurface and from unpatterned lithium niobate thin film. The metasurface provides 65 times enhancement to the SPDC rate and high signal-to-noise ratio.

The measurement indicates SPDC efficiencies of 75 mHz/mW and 1.15 mHz/mW for metasurface and unpatterned thin film, respectively, as shown in Fig. S4. As a result, the SPDC rate of the lithium niobate metasurface is found to be ∼65 times higher compared to an unpatterned thin film of the same size. This improvement is observed for a collection angle of 1.5 degrees and a spectral bandwidth of approximately 50 nm.

S3.3 Characteristics of the pump beam

Here we use a laser diode (FPL785P, Thorlabs) with a tunable wavelength from 779 nm to 791 nm to pump the nonlinear metasurface. The wavelength tuning is realized through the diode temperature, as shown in Fig. S5. The discontinuous dependence on the temperature is due to the mode-hopping of the laser diode. The yellow lines mark the diode temperatures of -5 deg, 14 deg and 36 deg, corresponding to the three wavelengths we have chosen for the all-optical scanning imaging, i.e., 780 nm, 784 nm, 790 nm. Due to the mode hopping, the selected wavelengths are unevenly distributed but ensure sufficient tuning range of the photon emission.

As we have discussed above, the larger beam diameter of the pump beam on the metasurface offers better imaging resolution. Since the size of the fabricated metasurface is 400 µm, we consider a beam diameter of 200 µm such that the whole area of the pump beam overlaps with the metasurface. It is feasible to fabricate a bigger metasurface and employ a larger pump beam size, which would further improve the imaging resolution.

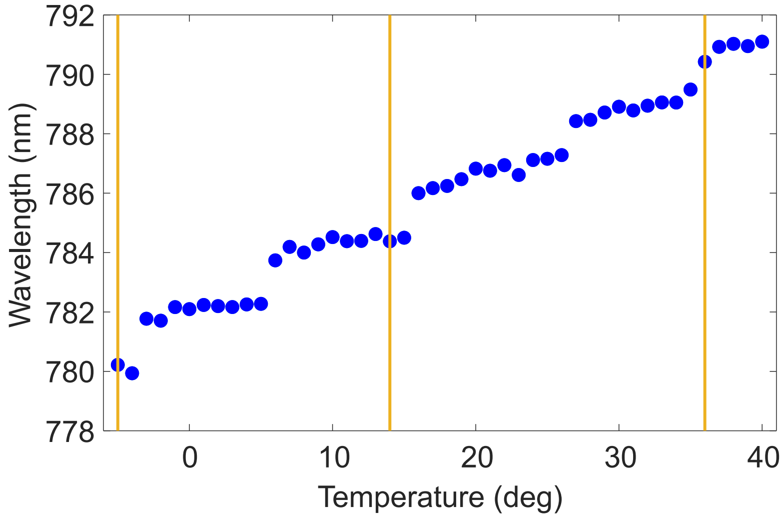

Figure S5 Pump beam wavelength as a function of laser temperature. The tuning of the pump beam wavelength is achieved by controlling the laser diode temperature. The yellow lines indicate the laser wavelengths we have selected for all-optical scanning imaging, i.e., 780 nm, 784 nm, and 790 nm. The wavelengths are extracted from the Gaussian fit of laser spectra measured with a spectrometer.

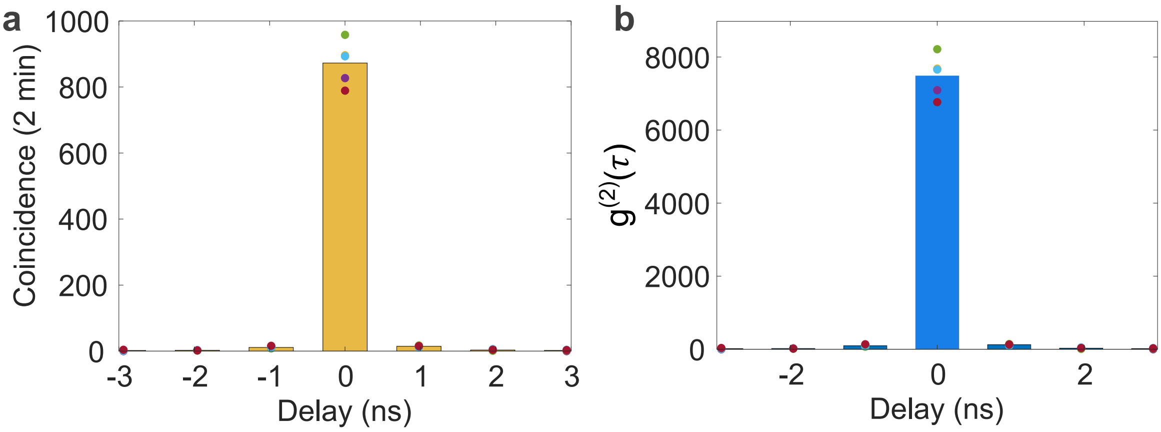

Figure S6 **a,** Measured coincidences of photon pairs from the nonlinear metasurface. The dots in different colors present five independent measurements used to calibrate the second-order correlation function and photon-pair rate shown in Fig. 2**b** of the main paper. The histogram illustrates the average coincidence values. **b,** Second-order correlation function $g^{(2)}(\tau)$ calibrated from the coincidence measurements.

S3.4 Coincidence measurement of photon pairs

The second-order correlation function $g^{(2)}(\tau)$ and photon-pair rate presented in Fig. 2**b** of the main paper are calibrated from five independent coincidence measurements, each lasting 2 minutes. Individual measurements are shown in Fig. S6 (dots in different colors).

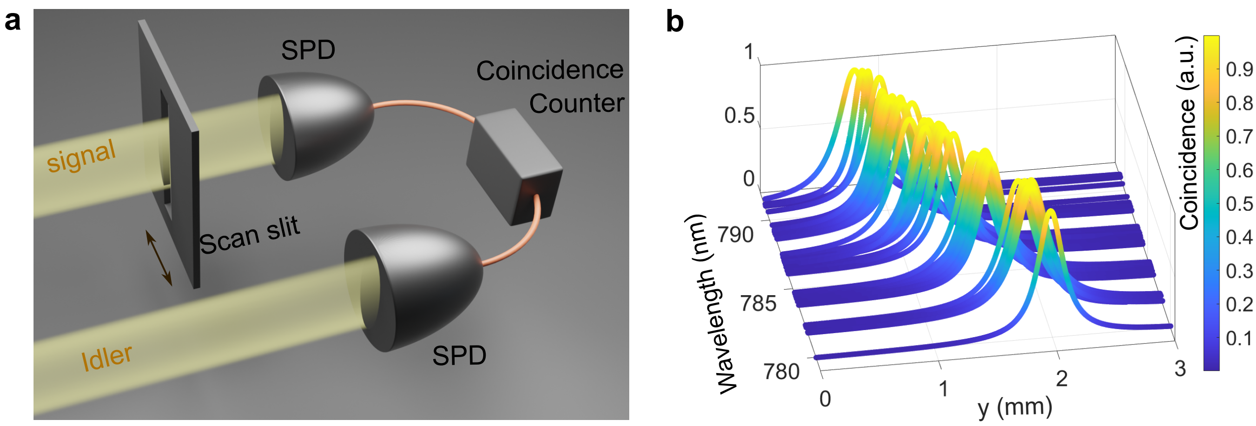

Figure S7 **a,** Experimental setup for optical scanning. The two single-photon detectors register the coincidence counts of the photon pairs from the metasurface, by translating a slit along the y-direction in the signal arm. The measurements are repeated at various pump wavelengths. **b,** Photon emission vs. pump wavelength. The emission pattern of photon pairs is calibrated from the coincidence measurements as a function of the slit position.

S3.5 Characterization of tunable emission

To achieve all-optical scanning imaging, we first experimentally characterize the tunable emission of the photon pairs from the nonlinear metasurface, as shown in Fig. S7**a**. After splitting the photon emission into signal and idler arms, a narrow slit is placed in the signal arm and is translated along the y-direction. The signal and idler photons are then collected with two single-photon detectors. We measure the coincidences of the photon pairs as a function of slit position at different pump wavelengths, with the measurement time of 2 minutes for each position.

To reconstruct the emission pattern from the coincidence measurement, we assume that the normalized emission profile P_y along the y-direction is Lorentzian, i.e., $P_y = a^2/(a^2 + (y - y_0)^2)$ (where a is a free parameter and y_0 denotes the peak position of the emission). The integral of P_y corresponds to the measured coincidence rate of the photon pairs, which is

$$C_{\mathrm{m}} = \int P_y dy = a \tan^{-1}\left(\frac{y - y_0}{a}\right). \tag{S5}$$

We perform a nonlinear fitting of the coincidence using Eq. (S5), allowing us to extract the parameters for the Lorentzian function of the emission. The calibrated emission pattern vs. pump wavelength is shown in Fig. S7**b**, where the emission shifts along the y-direction as the pump wavelength varies.

S4 Quantum object tracking

We propose a concept called "quantum object tracking", in which a moving object can be actively tracked using entangled photon pairs from the metasurface, as shown in the sketch in Fig. S8. Pumping the metasurface with a monochromatic laser triggers the emission of photon pairs at a specific direction along the y-axis. A moving object is illuminated with signal photons,

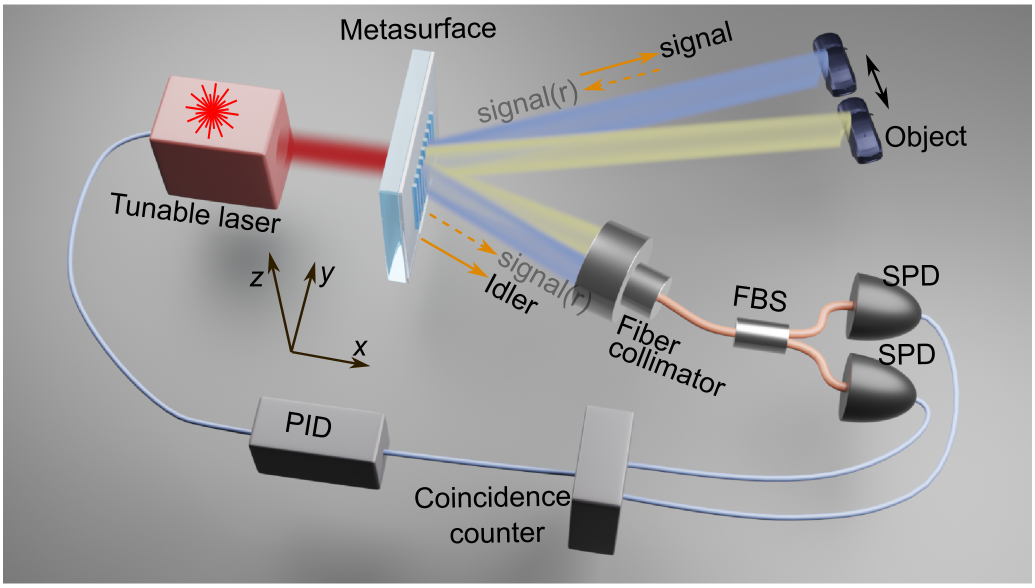

Figure S8 Concept of object tracking with photon-pair steering. The signal photons emitted from the metasurface are bounced back from a moving object and are then reflected by the same metasurface. The reflected signal photons combined with idler photons are collected with a fiber collimator and are then split into two optical paths using a fiber beam splitter (FBS). The signal and idler photons are collected by a pair of SPD. The real coincidence of the photon pairs is analyzed using the coincidence counter, which is further processed with a PID controller and fed to the tunable laser for controlling the laser wavelength and thereby the photon emission. Tracking the object is realized by finding the maximum of coincidence counts.

part of which are bounced back from the object and are then reflected by the same metasurface due to the optical resonances. The correlation of reflected signal photons and the idler photons is measured with single photon detectors and the coincidence counter. The coincidence signal processed with a PID controller is sent back to control the laser wavelength and thus the emission direction. If the object is moving away from the original position, the coincidence drops and the laser wavelength is automatically tuned to change the photon emission direction until maximum coincidence counts are achieved, thereby realizing the object tracking. The tracking speed is primarily limited by the rate of collected photon pairs, which can be substantially improved using detectors with better efficiency, metasurface materials with larger second-order nonlinearity, and improved metasurface design supporting higher optical quality factors.

S5 Comparison with a Fabry–Pérot cavity

To the best of our knowledge, the concept of quantum optical scanning imaging using the angular dispersion of optical resonances has not yet been proposed and demonstrated in previous works. Furthermore, we note that the dispersion in our metasurfaces is fundamentally different from that of a Fabry–Pérot cavity or any simple 2D optical resonator. The imaging protocol developed in this work with metasurfaces cannot be achieved with a Fabry–Pérot cavity.

To elaborate on this aspect, we consider a Fabry–Pérot cavity filled with a lithium niobate film. The angular dispersion for this system is described by $\lambda = 2n_{\mathrm{LN}}L\cos(\theta)/m$ (*S2*), where

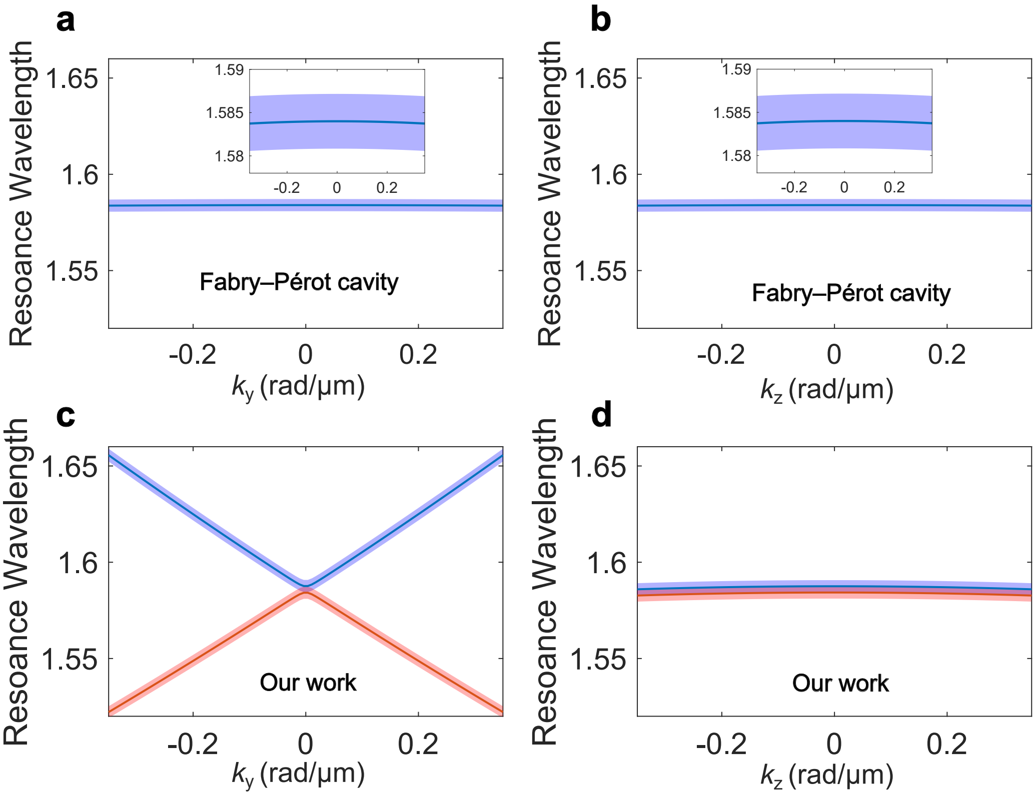

Figure S9 Angular dispersion of a Fabry–Pérot cavity and the metasurface developed in this work. a, Resonance wavelength of a Fabry–Pérot cavity vs. k_y at $k_z = 0$. **b,** Resonance wavelength of a Fabry–Pérot cavity vs. k_z at $k_y = 0$. **c,** Resonance wavelength of the metasurface vs. k_y at $k_z = 0$. **d,** Resonance wavelength of the metasurface vs. k_z at $k_y = 0$. The shaded areas represent the linewidth of resonance bands.

$\theta = \arcsin(n_0 \sin(\theta_0)/n_{\mathrm{Ln}})$ is the refraction angle inside the cavity. Here λ is the resonance wavelength, θ_0 is the incident angle, n_{LN} and n_0 are the refractive indices of lithium niobate and air, L is the length of the cavity, and m is a positive integer. This expression can be simplified to $\lambda = \lambda_0 \cos(\theta)$, where $\lambda_0 = 2n_{\mathrm{LN}}L/m$ is the resonance wavelength at normal incidence and is set to 1584 nm for comparison with our work. This angular dispersion is fundamentally different from the one of our metasurface. First, the dispersion in a Fabry–Pérot cavity is identical for both transverse directions due to the symmetry, as shown in Figs. S9a-b. Additionally, the resonance is nearly flat within the linewidth in both directions, assuming an optical Q of ~ 500 similar to that of our metasurface. This leads to a broad biphoton emission in k-space in both directions, significantly limiting the tunability of optical scanning imaging.

In contrast, the dispersion manifested in our metasurface is nearly linear in the y-direction and is close to flat in the z-direction (see Figs. S9c-d). As a result, the spatial correlations in the two directions are different (see Figs. 1d and 1e). It is these unique dispersion features and spatial correlations that enable the developed imaging protocol combining optical scanning imaging (y-direction) and quantum ghost imaging (z-direction).

S6 Comparison of different imaging techniques

In Table S2, we compare the imaging protocol developed in this work with established quantum ghost imaging and single-pixel computational ghost imaging.

Quantum ghost imaging (second column) allows low-dose illumination, high sensitivity in noisy environments, and imaging at non-degenerate wavelengths (*S3–S7*). Its resolution is determined by the spatial bandwidth of the pump beam since the measurement is based on the spatial correlation of entangled photon pairs.

Computational ghost imaging (third column) requires only one single-pixel detector and the image is reconstructed with computational algorithms based on the patterns of the incident light (*S8*, *S9*). The setup can be simple and flexible.

In this work, we develop a quantum optical scanning imaging protocol (first column) using photon pairs from a metasurface supporting optical resonances with a unique angular dispersion, where the emission direction of photon pairs can be tuned optically by changing the pump wavelength. Unprecedented imaging resolution can be potentially achieved with a million-Q metasurface (*S10*). Pumping the metasurface with a frequency comb may facilitate ultrafast scanning. Additionally, we combine this scanning protocol with traditional ghost imaging, facilitating novel quantum imaging with unique benefits.

Characteristic	Optical Scanning Imaging (this work)	Quantum Ghost Imaging (Refs. (*S3*–*S7*) and this work)	Single-Pixel Computational Ghost Imaging (*S8*, *S9*)
Imaging Method	Scan a focused light beam across the object point by point by adjusting the pump wavelength.	Illuminate the object with the signal photon and collect the photon with a single-pixel detector. Collect the idler photon with a detector array and reconstruct the image based on the spatial correlations of signal/idler photons.	Illuminate the object with structured light patterns, collect photons with a single-pixel detector, and reconstruct the image with the computational algorithm.
Complexity	Straightforward with pump wavelength tuning.	Require correlation detection.	Moderate complexity (simpler hardware, computationally intensive).
Resolution	Determined by the Q of metasurface resonances. Unprecedented resolution can be potentially achieved with a million-Q metasurface demonstrated recently (*S10*).	Determined by spatial correlations, as determined by the pump beam radius.	Dependent on the number of structured patterns used and computational power.
Speed	Can be potentially ultra-fast with a frequency comb.	Slow due to photon correlation measurements.	Slow for high resolution, requires multiple illumination patterns.
Unique benefits	Precise Control. Low-dose illumination. Potential for high spatial resolution and high speed.	Low-dose illumination, avoiding damage to samples. High sensitivity in noisy environments. Allow imaging at non-degenerate wavelength	Only need a single-pixel detector. Flexible illumination

Table S2 Comparison of Imaging Methods

References

S1. Zhang, J.H., Ma, J.Y., Parry, M., Cai, M., Camacho-Morales, R., Xu, L., Neshev, D.N., Sukhorukov, A.A.: Spatially entangled photon pairs from lithium niobate nonlocal metasurfaces. Sci. Adv. **8**(30), 4240 (2022) https://doi.org/10.1126/sciadv.abq4240

S2. Lipson, S., Lipson, H., Tannhauser, D.: Optical physics 3rd ed. (Cambridge University Press, Cambridge, 1998) (1995) https://doi.org/10.1017/CBO9781139170413

S3. Morris, P.A., Aspden, R.S., Bell, J.E.C., Boyd, R.W., Padgett, M.J.: Imaging with a small number of photons. Nature Communications **6**(1), 5913 (2015) https://doi.org/10.1038/ncomms6913

S4. Padgett, M.J., Boyd, R.W.: An introduction to ghost imaging: quantum and classical. Philos. Trans. R. Soc. A **375**(2099), 20160233 (2017) https://doi.org/10.1098/rsta.2016.0233

S5. Vega, A., Saravi, S., Pertsch, T., Setzpfandt, F.: Pinhole quantum ghost imaging. Applied Physics Letters **117**(9), 094003 (2020) https://doi.org/10.1063/5.0012477

S6. Moreau, P.-A., Toninelli, E., Morris, P.A., Aspden, R.S., Gregory, T., Spalding, G., Boyd, R.W., Padgett, M.J.: Resolution limits of quantum ghost imaging. Optics Express **26**(6), 7528 (2018) https://doi.org/10.1364/OE.26.007528

S7. Vega, A., Pertsch, T., Setzpfandt, F., Sukhorukov, A.A.: Metasurface-Assisted Quantum Ghost Discrimination of Polarization Objects. Physical Review Applied **16**(6), 064032 (2021) https://doi.org/10.1103/PhysRevApplied.16.064032

S8. Shapiro, J.H.: Computational ghost imaging. Physical Review A **78**(6), 061802 (2008) https://doi.org/10.1103/PhysRevA.78.061802

S9. Erkmen, B.I., Shapiro, J.H.: Ghost imaging: From quantum to classical to computational. Advances in Optics and Photonics **2**(4), 405 (2010) https://doi.org/10.1364/AOP.2.000405

S10. Fang, J., Chen, R., Sharp, D., Renzi, E.M., Manna, A., Kala, A., Mann, S.A., Yao, K., Munley, C., Rarick, H., Tang, A., Zheng, Y., Menon, V.M., Alù, A., Majumdar, A.: Million-Q Free Space Meta-Optical Resonator at Visible Wavelengths https://doi.org/10.48550/arXiv.2409.02874